

RESEARCH ARTICLE

10.1002/2017JA024634

Key Points:

- The electron densities at the crests of the equatorial ionization anomaly in 2003 and 2014 were 3 times higher than that in 2009
- The equatorial ionization anomaly moved poleward by $\sim 10^\circ$ and was more pronounced in the northern hemisphere during 2014
- The altitude of the maximal 27 day solar response is ~ 50 km higher than that of the 11 year solar response

Correspondence to:

M.-C. Liang,
mcl@rcec.sinica.edu.tw

Citation:

Li, K.-F., Lin, L.-C., Bui, X.-H., & Liang, M.-C. (2018). The 11 year solar cycle response of the equatorial ionization anomaly observed by GPS radio occultation. *Journal of Geophysical Research: Space Physics*, 123, 848–861. <https://doi.org/10.1002/2017JA024634>

Received 28 JUL 2017

Accepted 12 DEC 2017

Accepted article online 18 DEC 2017

Published online 23 JAN 2018

The 11 Year Solar Cycle Response of the Equatorial Ionization Anomaly Observed by GPS Radio Occultation

King-Fai Li^{1,2} , Li-Ching Lin³ , Xuan-Hien Bui^{3,4} , and Mao-Chang Liang^{3,4,5} 
¹Department of Applied Mathematics, University of Washington, Seattle, WA, USA, ²Department of Environment Sciences, University of California, Riverside, CA, USA, ³Research Center for Environmental Changes, Academia Sinica, Taipei, Taiwan, ⁴Taiwan International Graduate Program-Earth System Science Program, Academia Sinica and National Central University, Taoyuan, Taiwan, ⁵Graduate Institute of Astronomy, National Central University, Jhongli, Taiwan

Abstract We have retrieved the latitudinal and vertical structures of the 11 year solar cycle modulation on ionospheric electron density using 14 years of satellite-based radio occultation measurements utilizing the Global Positioning System. The densities at the crests of the equatorial ionization anomaly (EIA) in the subtropics near 300 km in 2003 and 2014 (high solar activity with solar 10.7 cm flux, $F_{10.7} \approx 140$ solar flux unit (sfu)) were 3 times higher than that in 2009 (low solar activity $F_{10.7} \approx 70$ sfu). The higher density is attributed to the elevated solar extreme ultraviolet and geomagnetic activity during high solar activity periods. The location of the EIA crests moved ~ 50 km upward and $\sim 10^\circ$ poleward, because of the enhanced $\mathbf{E} \times \mathbf{B}$ force. The EIA in the northern hemisphere was more pronounced than that in the southern hemisphere. This interhemispheric asymmetry is consistent with the effect of enhanced transequatorial neutral wind. The above observations were reproduced qualitatively by the two benchmark runs of the Thermosphere-Ionosphere-Electrodynamics General Circulation Model. In addition, we have studied the impact of the 11 year solar cycle on the 27 day solar cycle response of the ionospheric electron density. Beside the expected modulation on the amplitude of the 27 day solar variation due to the 11 year solar cycle, we find that the altitude of the maximal 27 day solar response is unexpectedly ~ 50 km higher than that of the 11 year solar response. This is the first time that a vertical dependence of the solar responses on different time scales is reported.

1. Introduction

Ionospheric electrons are produced from ionization of molecules and atoms by solar extreme ultraviolet (EUV) (above 100 km) and X-ray (below 100 km). Large changes in solar radiation and geomagnetic activity affect the production of free electrons in the ionosphere (60–2000 km) (Baron et al., 1983; Forbes et al., 2000; Rishbeth & Mendillo, 2001), leading to significant impacts on, for example, civil radio communication (Kutiev et al., 2012; Wells, 1943) and satellite orbital stability (Walterscheid, 1989). Solar-induced variations in the ionospheric electron density have been monitored routinely (Afraimovich et al., 2008; Appleton & Naismith, 1940; Baron et al., 1983; Bartels, 1950; Handzo et al., 2014; Huang et al., 2015; Lei et al., 2008; Liang et al., 2008; Ma et al., 2012; Munro, 1962; Pedatella et al., 2010) and incorporated in ionospheric models for space weather forecasts (Bilitza et al., 2011; Hochegger et al., 2000; Jakowski et al., 2011; Scherliess et al., 2004; Wang et al., 2016; Yue et al., 2012).

One pronounced effect of the solar cycle influence in ionospheric electron density is the equatorial ionization anomaly (EIA) (Appleton, 1946; Namba & Maeday, 1939). The EIA is a feature of the nonuniform latitudinal distribution in ionospheric electron density, exhibiting two crests at magnetic latitudes around 15° north/south and a trough at the magnetic dip equator. The EIA is a result of the fountain effect, where ionized particles at low altitudes in the ionosphere away from the magnetic equator are uplifted by the $\mathbf{E} \times \mathbf{B}$ dynamo electric field (Bramley & Peart, 1965; Duncan, 1960; Fejer, 1964; Hanson & Moffett, 1966; Martyn, 1955; Rishbeth, 1997) and then diffuse downward and poleward along the geomagnetic lines (Kendall, 1962; Mitra, 1946). The location and magnitude of the EIA subtropical crests may also be affected by the transequatorial neutral wind (Balan et al., 2013; Hanson & Moffett, 1966; Nanan et al., 2012). We refer to, for example, Rishbeth (2000) for a historical review of the EIA.

Previous studies have reported the solar influence on the total electron content (TEC) (e.g., see Alizadeh et al., 2011; Araujo-Pradere et al., 2011; Bergeot et al., 2013; Garner et al., 2008; Huang & Cheng, 1996; Ikubanni & Adeniyi, 2017; Kumar et al., 2014, 2016). For example, Huang and Cheng (1996) studied the variations of TEC over Taiwan and showed a clear correlation between the 11 year solar cycle and the TEC: the TEC at the EIA crests increased from ~ 0.4 TEC unit (TECU, 1 TECU = 1×10^{16} el m $^{-2}$) during the solar minimum in 1986 to ~ 1 TECU during the solar maximum in 1990. They also showed in their Figure 3 that the latitude of the EIA crest (hereafter denoted by $\theta_m F_2$) during solar maximum moved $\sim 1.5^\circ$ poleward relative to that during solar minimum, although they noted that the uncertainty of $\theta_m F_2$ was too large to establish the statistical significance of such a poleward movement. Kumar et al. (2014) also found an EIA movement by 4° poleward over India. So far, there has not been any detailed modeling study of the solar cycle-induced EIA poleward movement.

The EIA exhibits interhemispheric asymmetry (Vila, 1971). Mikhailov and Perrone (2015) show that the increase of EUV in January due to the decrease of the Sun-Earth distance at the perihelion results in 20% higher electron density in the northern EIA crest than in the southern EIA crest. In addition, the transequatorial neutral wind from the summer hemisphere to the winter hemisphere increases the electron density at the crest of the winter hemisphere (Lin et al., 2005). On decadal time scales, Luan et al. (2015) showed that the winter hemispheric EIA crest is further enhanced during the 2012 high solar activity period (see their Figure 5). A magnified EIA interhemispheric asymmetry due to the geomagnetic storm was also evident in Lin et al.'s (2005) simulation.

We note that previous studies mostly focus on either the TEC (e.g., see Huang & Cheng, 1996; Kumar et al., 2014, 2016) or the density at the crests (denoted by $N_m F_2$ in the literature) (e.g., see Chen & Liu, 2010; Liu et al., 2006). For example, Luan et al. (2015) studied the interannual variability induced by the 11 year solar cycle using the Global Positioning System (GPS) measurements derived from the joint Taiwan-U.S. Formosa Satellite Mission-3/Constellation Observing System for Meteorology, Ionosphere and Climate (FORMOSAT-3/COSMIC). However, they limited their study to quantities such as $N_m F_2$ and the altitude of the crests (denoted by $h_m F_2$ in the literature). To our knowledge, there have not been studies focusing on the global structures of the 11 year solar cycle response in the ionospheric electron density.

Our purpose here is to report the latitudinal-vertical two-dimensional (2-D) structure of the 11 year solar cycle response in the ionosphere using the electron density retrieved from GPS radio occultation (RO). This satellite-based data set allows us to reexamine the EIA variations (such as poleward movements of the EIA crests and the EIA interhemispheric asymmetry) that were previously reported from ground-based and ionosonde observations. We will also extend the work of Liang et al. (2008) to examine the 2-D structure of the 27 day solar cycle response. Compared to previous studies, we simplify the analysis with annual and zonal averages to effectively remove the strong seasonal and diurnal dependence of the 11 year solar response, as well as the zonal variations due to atmospheric tides and planetary waves (see more discussions in section 2). Finally, two benchmark runs of the Thermosphere Ionosphere Electrodynamics General Circulation Model (TIE-GCM) at solar maximum and minimum conditions will be used to provide a brief assessment of the direct solar forcing on the response of the ionospheric electron density.

We organize the paper as follows: section 2 describes the satellite data used. Section 3 discusses the vertical structures of the 11 year and 27 day solar cycle responses. We summarize our findings in section 4.

2. Data

The ionospheric electron density was retrieved by the Abel transform of the measured delay of GPS RO signals (Jakowski et al., 2007; Pedatella et al., 2015; Shaikh et al., 2014; Yue et al., 2014). We use three GPS RO measurements: Germany's Challenging Mini-satellite Payload (CHAMP) (Yue et al., 2011), United States' Gravity Recovery and Climate Experiment (GRACE) (Tapley et al., 2004), and the FORMOSAT-3/COSMIC (Syndergaard et al., 2006).

CHAMP, a single-satellite mission, was launched in 2000 into a near-polar orbit at 454 km and slowly descended to 300 km near the end of the mission in 2010 (Yue et al., 2011). On average, 80–90 vertical electron density profiles above 100 km were retrieved daily from the CHAMP. GRACE, in a near-polar orbit, also provided RO data for ionospheric electron density retrieval (Tapley et al., 2004). Another data set of GRACE

Table 1

High Solar Activity (HSA) and Low Solar Activity (LSA) Periods Defined for CHAMP, GRACE, and FORMOSAT-3/COSMIC Measurements, With the Associated $F_{10.7}$ Values Averaged Over the Referred Time Periods in the Brackets

	HSA period (averaged $F_{10.7}$)	LSA period (averaged $F_{10.7}$)
CHAMP	Jan–Dec 2003 (130 sfu)	Jan–Dec 2007 (73 sfu)
GRACE and COSMIC	Apr 2014 to Mar 2015 (139 sfu)	Jan–Dec 2009 (70 sfu)
TIE-GCM model	Benchmark run (200 sfu)	Benchmark run (70 sfu)

Note. The $f_{10.7}$ values for the benchmark runs of the TIE-GCM simulations performed at solar maximum and solar minimum conditions are also displayed.

electron density profiles retrieved using microwave measurements between the twin instruments (Xiong et al., 2010) is not used in this study. FORMOSAT-3/COSMIC (Syndergaard et al., 2006) consists of six microsatellites, which were launched in 2006 into 72° orbits at 512 km. About 1,000–1,500 vertical electron density profiles between 100 km and 500 km were retrieved daily from the FORMOSAT-3/COSMIC measurements. Overall, the number of daily retrievals provided by FORMOSAT-3/COSMIC is a factor of ~10 times more than those by CHAMP and GRACE.

All the RO data used in this work are obtained from <http://www.cosmic.ucar.edu/>. For consistency and long-term data integrity and stability, postprocessed swath data products “ionprf” from the National Center for Atmospheric Research (Colorado, USA) are used in this work: CHAMP (code name: champ2014, covering 2002–2008), GRACE (code name: grace, covering 2007–2016), and FORMOSAT-3/COSMIC (code names: cosmic2013 and cosmic, covering, respectively, 2006–2014 and 2014–2016). In total, ~5 million occultation profiles are analyzed in this study. Below, we focus on the 27 day and 11 year solar responses in the ionosphere using these RO data sets.

The 11 year solar cycle may indirectly affect the ionospheric electron density distribution through modulation of atmospheric tides. Nonmigrating tides (relative to the Earth), resulting from longitudinally asymmetric surface topography, create diurnal tides at low- and middle-latitudes in the ionosphere (Forbes et al., 2008). The amplitudes of these tides are larger during solar maximum (Jones et al., 2013) than at solar minimum, but the normalized amplitudes relative to the zonal mean remain unchanged (Zhou et al., 2016), suggesting that the solar cycle effect in the ionosphere can be studied effectively using the zonal mean. To simplify our analysis, we zonally and diurnally average the CHAMP, GRACE, and FORMOSAT-3/COSMIC data to extract the effects of the 11 year solar cycle; the longitudinal dependence of the solar modulation will not be studied in the work. The zonal and daily averaging also helps remove the diurnal and semidiurnal tides associated with seasonal cycles and the El Niño–Southern oscillation (Pedatella & Liu, 2013). The electron density profiles are averaged diurnally and zonally into 36 latitude bins (2° wide) pole-to-pole, with latitude grids centering at 89°S, 87°S, ..., 89°N. The data are further averaged vertically into 41 layers (10 km thick) from 100 km to 510 km, with vertical grids centering at 105 km, 115 km, ..., 505 km. In this vertical range, the signal is significantly greater than noise level (Anthes et al., 2008; Schreiner et al., 2007).

As an application, we compare the observed 11 year solar cycle responses with the TIE-GCM modeled response (Dickinson et al., 1981, 1984; Roble et al., 1988; Solomon & Qian, 2005; Solomon et al., 2013). The TIE-GCM version 2.0 and its benchmark runs were obtained from <http://www.hao.ucar.edu/modeling/tgcm/>. This model at 2.5° resolution provides two benchmark runs at solar maximum and minimum conditions corresponding to the 10.7 cm radio fluxes, $F_{10.7}$, 200 sfu and 70 sfu, respectively ($1 \text{ sfu} = 10^{-22} \text{ W m}^{-2} \text{ Hz}^{-1}$). The bottom and top levels in the model are 5.48×10^{-4} hPa and 4.56×10^{-10} hPa. Since the observed electron density is specified on geometric altitudes, the TIE-GCM pressure levels are converted to geometric altitudes before the comparison. We note that quantitative differences between observations and the TIE-GCM benchmark runs presented below may be partially attributed to the bias of the model setups, such as the solar forcing (Table 1) and the lower boundary conditions. The latter may lead to different dynamical responses in the ionosphere: Jones et al. (2016) showed that the dissipation of upward propagating tides originated from the model lower boundary induced ~30% and ~10% reduction in $N_m F_2$ during high and low solar activity periods, respectively. Despite these biases, we show that the comparison of the observations with the benchmark runs still provides useful insights into the EIA and solar cycle dependence of ionospheric electron densities.

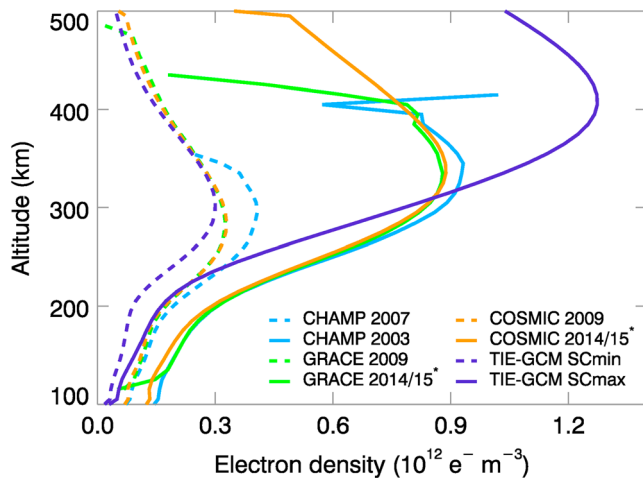


Figure 1. Comparison of the vertical electron density profiles at different solar phases observed by CHAMP, GRACE, and FORMOSAT-3/COSMIC. The TIE-GCM benchmark simulation results are also shown. The asterisk indicates that the high solar activity period for GRACE and FORMOSAT-3/COSMIC observations is defined from April 2014 to March 2015; other high and low solar activity periods for the individual instrument are defined in Table 1.

demonstrate a dominant role of the direct solar forcing to the decadal variability in the ionospheric electron density, consistent with the conclusion arrived by, for example, Solomon et al., (2013). A more sophisticated and quantitative assessment requires a dedicated modeling performed with realistic boundary and forcing conditions (e.g., see Jones et al., 2016), which is beyond the scope of the current work.

Figure 2 compares the tropical means of the electron densities at 305 km (near the peak) measured by CHAMP (cyan line), GRACE (green line), and FORMOSAT-3/COSMIC (orange line). The diurnally averaged $F_{10.7}$ is also shown (red line) to illustrate the solar variability. Of the three measurements, the FORMOSAT-3/COSMIC time series has the smallest short-term (<1 year) variability

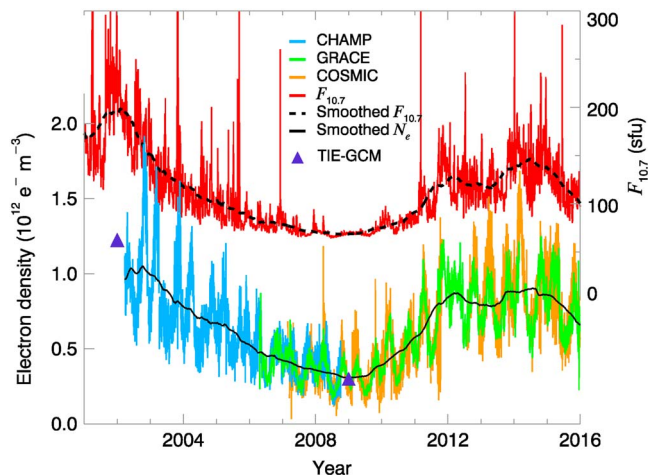


Figure 2. Tropical average (25°S–25°N) of daily electron densities at 305 km measured by CHAMP (cyan), GRACE (green), and FORMOSAT-3/COSMIC (orange). To show the 11 year solar cycle variability, the 10.7 cm radio flux ($F_{10.7}$) is overlaid. One solar flux unit (sfu) = $10^{-22} \text{ W m}^{-2} \text{ Hz}^{-1}$. The solid and dashed lines are the 1 year running averages of the merged electron density and $F_{10.7}$ solar index, respectively. The two benchmark runs of TIE-GCM, corresponding to $F_{10.7} = 200$ sfu and 70 sfu, are shown by the triangles. For a fair comparison, the equatorial average ($\sim 1.2 \times 10^{12} \text{ el m}^{-3}$) of the solar maximum run at 405 km, rather than 305 km, is reported (see text for details).

3. Results

3.1. Tropical Averages

Figure 1 compares the vertical profiles of the tropical mean (25°S–25°N) electron density in different solar cycle phases. The low solar activity year for GRACE and FORMOSAT-3/COSMIC is defined as January–December 2009, and the high solar activity year is defined as April 2014–March 2015 (due to missing FORMOSAT-3/COSMIC data in the first 3 months of 2014). For CHAMP, limited by the time coverage as well as the descending orbit, we take January–December 2003 and 2007 to represent the high and low solar activity years, respectively (Table 1). In 2007, the tropical electron density attains a maximum value of $\sim 0.4 \times 10^{12} \text{ el m}^{-3}$ at 290 km, whereas in 2003, the tropical electron density shows the maximum value of $\sim 0.9 \times 10^{12} \text{ el m}^{-3}$ at 340 km. The TIE-GCM benchmark runs are plotted for comparison. The maximum electron density of the solar minimum run agrees well with the observations. In the solar maximum run, the maximum electron density $N_m F_2$ is $\sim 40\%$ more than the observed in 2003 by CHAMP and in 2014 by GRACE and COSMIC. This can be explained by the fact that the input $F_{10.7}$ value in the TIE-GCM benchmark run is 50% greater than the reported $F_{10.7}$ for 2003 and 2014. The altitude of the maximum electron density for the solar maximum run is also higher at ~ 410 km. These benchmark runs

show a dominant role of the direct solar forcing to the decadal variability in the ionospheric electron density, consistent with the conclusion arrived by, for example, Solomon et al., (2013). A more sophisticated and quantitative assessment requires a dedicated modeling performed with realistic boundary and forcing conditions (e.g., see Jones et al., 2016), which is beyond the scope of the current work.

Figure 2 compares the tropical means of the electron densities at 305 km (near the peak) measured by CHAMP (cyan line), GRACE (green line), and FORMOSAT-3/COSMIC (orange line). The diurnally averaged $F_{10.7}$ is also shown (red line) to illustrate the solar variability. Of the three measurements, the FORMOSAT-3/COSMIC time series has the smallest short-term (<1 year) variability due to more spatial/temporal samplings that help average out the zonal and temporal variations in the tropical mean. The decadal variations in the zonally averaged electron density and $F_{10.7}$ are better seen with the 1 year running averages, which are shown by the solid and dashed black lines, respectively. The decadal variation in the zonally averaged electron density closely follows that of $F_{10.7}$: the electron density dropped from a relatively high value of $1.0 \times 10^{12} \text{ el m}^{-3}$ in 2003 to $0.3 \times 10^{12} \text{ el m}^{-3}$ during 2008–2009 and increased to $0.8 \times 10^{12} \text{ el m}^{-3}$ in 2012. Then it stayed on a plateau until 2014 and decreased again after 2014. The TIE-GCM benchmark run values are plotted as the purple triangles in 2002 and 2009. The solar minimum run produces the equatorial average of $0.3 \times 10^{12} \text{ el m}^{-3}$ at 305 km, close to the GRACE and FORMOSAT-3/COSMIC observations in 2009. For the comparison, the equatorial average ($\sim 1.2 \times 10^{12} \text{ el m}^{-3}$) of the solar maximum run at 405 km where the electron density maximizes, rather than 305 km, is shown.

3.2. Latitudinal Patterns

Next we compare the latitudinal patterns of the observed and modeled electron densities during the high and low solar activity periods defined in Table 1 (Figure 3). To account for the difference in the $F_{10.7}$ values during the years when the observations were taken and the value used in the model, we scale the electron density of the TIE-GCM run at the solar

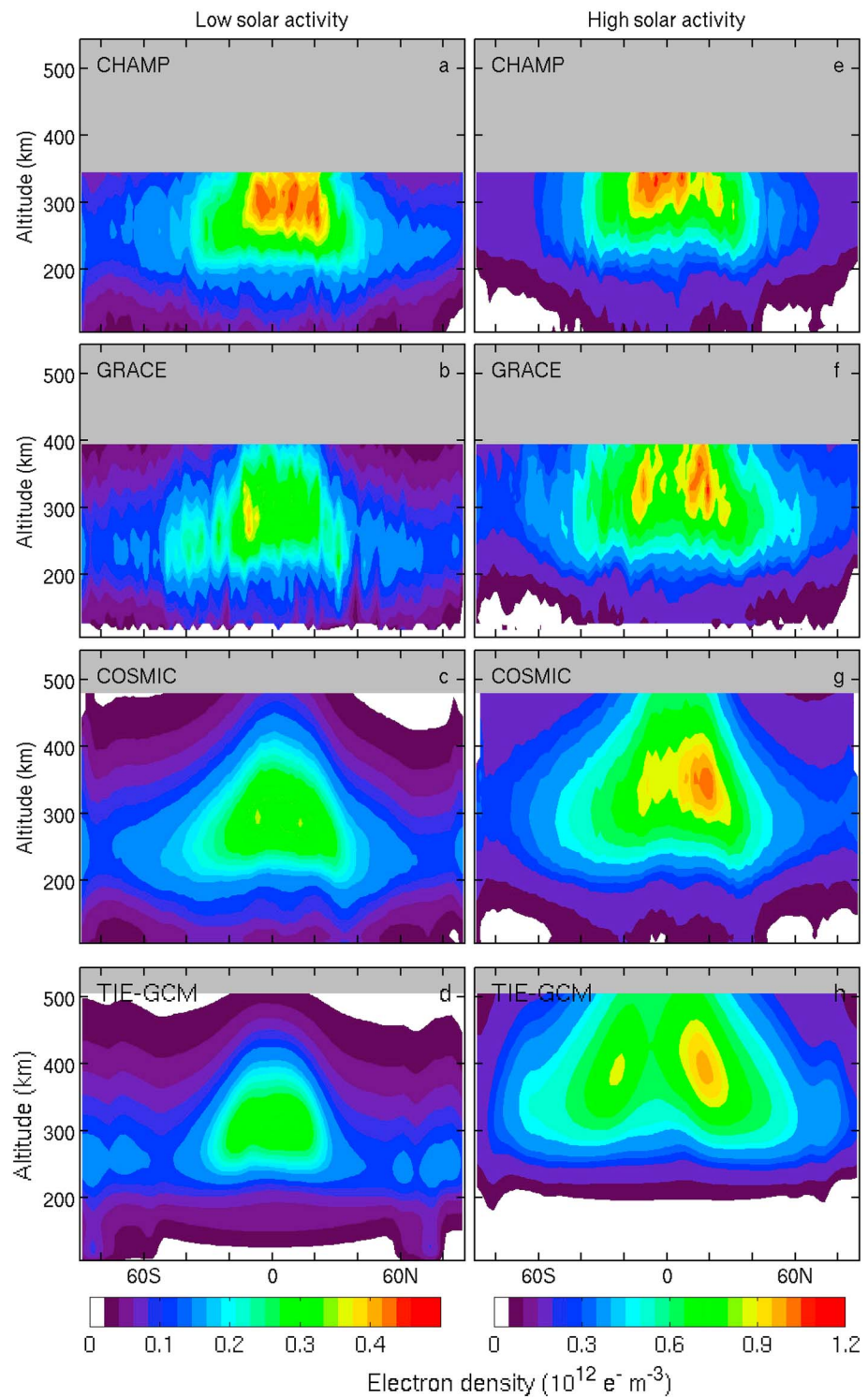


Figure 3. Ionospheric electron density observed in high and low solar activity periods defined in Table 1. Note that the color scales for the left and right columns are different. Grey shades represent missing data. For comparison, the TIE-GCM simulations are shown at the bottom.

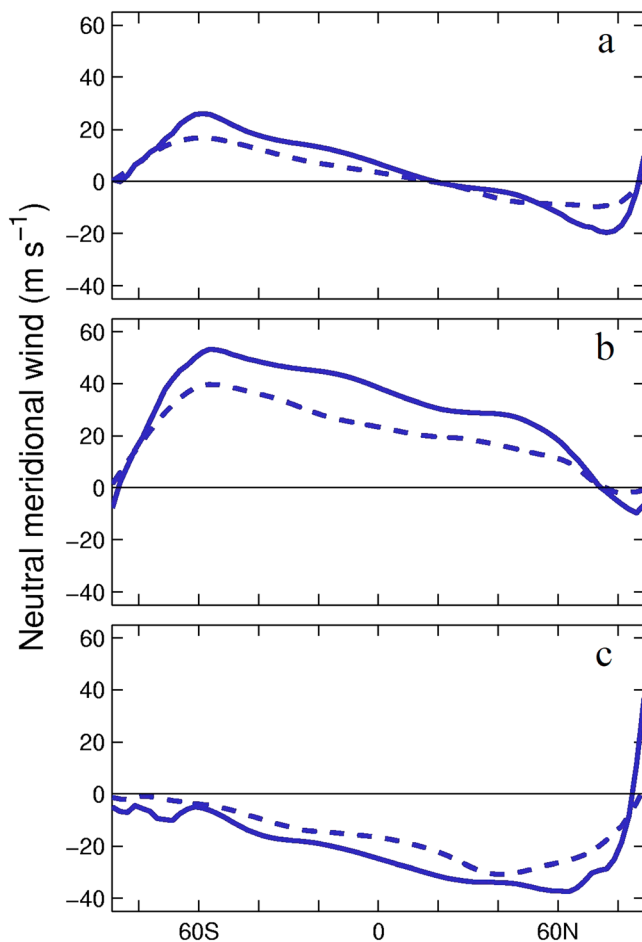


Figure 4. Neutral meridional wind (m s^{-1}) from the two TIE-GCM benchmark runs, at the EIA peak altitudes of 310 km (solar minimum; dashed curve) and 390 km (solar maximum; solid curve). (a) Annual average, (b) winter solstice (January), and (c) summer solstice (July). Positive values refer to northward flow.

scale, we show the annually averaged neutral meridional wind in Figure 4a. Although the neutral meridional wind reverses from one season to the other (Figures 4b and 4c), the magnitudes of wind speeds are not the same. Therefore, when annually averaged, the net transequatorial flow (i.e., the meridional wind at the equator) is northward, in both the solar maximum and solar minimum runs. This northward meridional wind extends to 20°N , beyond which the southward meridional wind dominates. The net northward transequatorial wind is stronger during solar maximum, thereby strengthening the EIA interhemispheric asymmetry.

The EIA interhemispheric asymmetry in the CHAMP (Figure 3e) appears differently from that in the GRACE and FORMOSAT-3/COSMIC observations. The CHAMP observation shows a higher electron density in the southern hemisphere during the post solar maximum period in 2003, in contrast to the other two data sets and the TIE-GCM simulation that possess an enhanced distribution in the northern hemisphere. We do not know whether this reversed asymmetry is a consequence of two different solar cycles 23 and 24, although the values of $F_{10.7}$ in the selected years (2003 and 2014) are comparable (see Table 1). Extended GPS radio occultation over future solar cycles would help resolve this issue.

3.3. EIA Sensitivities

The patterns described above are used to examine the changes of the EIA crests over the solar cycle. Quantities of interest here include $N_m F_2$, $h_m F_2$, and $\theta_m F_2$ at the EIA crests. Note that since the GPS RO data have been annually averaged, the seasonal variability of these quantities will not be examined here.

maximum by a factor of 0.65, for a better comparison. We note that such a scaling does not impair the evaluation between the model and data. Previous observations suggested that the increase of $N_m F_2$ saturates at $F_{10.7}$ greater than 200 sfu (Balan et al., 1993), beyond which the linearity assumption no longer holds. The $F_{10.7}$ value (200 sfu) used in the TIE-GCM solar maximum run is at the upper limit of the linearity, and we assume that the saturation effect is negligible at this $F_{10.7}$ value. Moreover, because the rate coefficients for photodissociation and photoionization are parameterized linearly with $F_{10.7}$ (Solomon & Qian, 2005), we do not expect the saturation effect to be significant in the model (see also Balan et al., 1993 for a discussion on the relationship between the solar $F_{10.7}$ and EUV fluxes).

One prominent pattern in Figure 3 is the presence of EIA, in which the electron densities at the crests vary with the solar activity. During the low solar activity period (Figures 3a–3d), the maximum electron density of GRACE, FORMOSAT-3/COSMIC, or TIE-GCM is $0.3\text{--}0.4 \times 10^{12} \text{ el m}^{-3}$ at the northern EIA crest; CHAMP gives $0.4\text{--}0.5 \times 10^{12} \text{ el m}^{-3}$. During the high solar activity period (Figures 3e–3h), the maximum value derived from CHAMP, GRACE, FORMOSAT-3/COSMIC, and the TIE-GCM is all consistent at $1.1\text{--}1.2 \times 10^{12} \text{ el m}^{-3}$.

There is a strong EIA interhemispheric asymmetry during high solar activity in GRACE, FORMOSAT-3/COSMIC, and TIE-GCM electron densities (Figures 3f–3h). The observed northern hemispheric EIA crest is 10%–15% more pronounced than the southern hemispheric one. This asymmetry is even more prominent in the TIE-GCM, with $\sim 30\%$ stronger in the northern hemisphere due to the higher solar flux input. Lin et al.'s (2005) simulations may provide a hint of the origin of the EIA interhemispheric asymmetry over the 11 year solar cycle, although their focus was on solar storm events. They studied the effects of (i) the storm $\mathbf{E} \times \mathbf{B}$ force and (ii) the transequatorial neutral wind associated with storm events, showing that a strong strengthening in the northern EIA crest due to the strengthened northward transequatorial wind perturbation. To demonstrate that the transequatorial neutral wind may also be a cause of the interhemispheric asymmetry on the 11 year solar cycle time

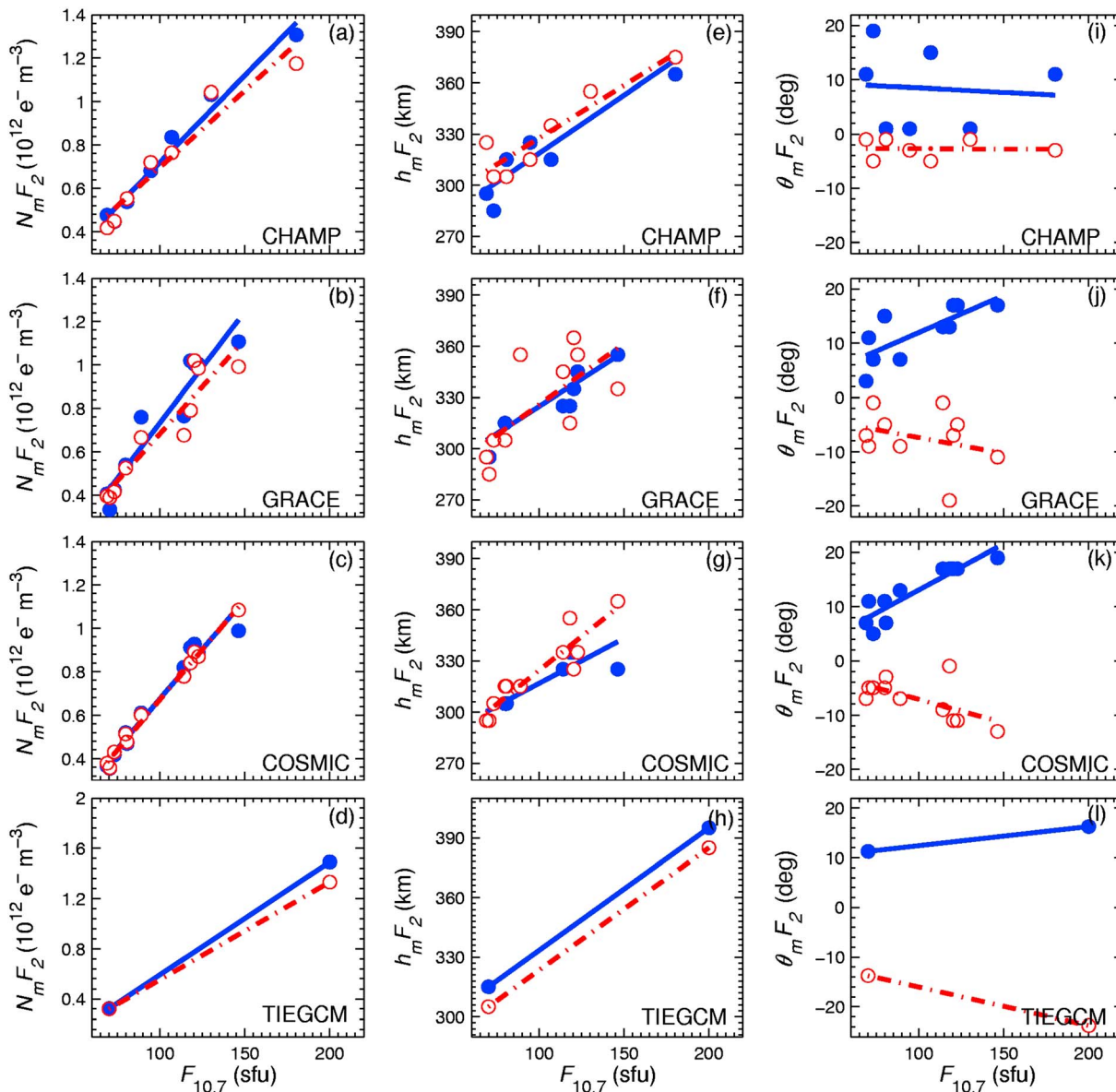


Figure 5. The annual averages of the (a–d) electron density (in the unit of $10^{12} \text{ el m}^{-3}$), (e–h) altitude (in the unit of km), and (i–l) latitude (in the unit of degrees) at the EIA crests plotted against the annually averaged $F_{10.7}$. Filled circles correspond to the northern hemispheric EIA crest, and open circles correspond to the southern hemispheric EIA crest. For CHAMP, GRACE, and COSMIC, the solid and dash-dotted lines are the linear regressions of the filled and open symbols, respectively. For TIEGCM, the points are connected with solid and dash-dotted lines to aid the comparisons with CHAMP, GRACE, and COSMIC observations.

Hereafter, we define the solar cycle sensitivity of a quantity as the change of that quantity per 100 sfu change in $F_{10.7}$. This unit (per $100F_{10.7}$) has been widely used in the studies of atmospheric responses to the solar cycles (Gray et al., 2010; Li et al., 2016), implicitly assuming that the thermospheric composition and temperature respond to the solar variability linearly (e.g., see Jones et al., 2016). This linear sensitivity assumption simplifies the comparison of climate responses at different solar cycles, where the total change in $F_{10.7}$ over individual cycles may not be the same. The saturation of $N_m F_2$ mentioned in section 3.2 would introduce non-linearity in the climate response when $F_{10.7}$ exceeds 200 sfu (Balan et al., 1993). However, during our observational periods, the annually averaged values of $F_{10.7}$ were between ~ 40 and 140 sfu and were well below the saturation limit. Therefore, we assume that the saturation effect was not significant in the observational data presented in this work. Furthermore, as discussed in section 3.2, the saturation effect in the TIE-GCM solar

Table 2

Solar Cycle Sensitivities of the Density ($\frac{dN_m F_2}{dF_{10.7}}$), Altitude ($\frac{dh_m F_2}{dF_{10.7}}$), and Latitude ($\frac{d\theta_m F_2}{dF_{10.7}}$) of the EIA Crests in the Northern and Southern Hemisphere, in the Unit of 10^{12} el $m^{-3}/100F_{10.7}$, km/100 $F_{10.7}$, and $^{\circ}N/100F_{10.7}$, respectively

Instruments	$\frac{dN_m F_2}{dF_{10.7}}$		$\frac{dh_m F_2}{dF_{10.7}}$		$\frac{d\theta_m F_2}{dF_{10.7}}$	
	North	South	North	South	North	South
CHAMP	0.80 ± 0.12	0.71 ± 0.18	68.1 ± 26.8	61.9 ± 22.9	-1.6 ± 17.0	-0.1 ± 4.1
GRACE	1.02 ± 0.21	0.87 ± 0.22	63.9 ± 34.8	71.5 ± 50.1	13.7 ± 7.7	-5.9 ± 12.0
COSMIC	0.91 ± 0.12	0.92 ± 0.06	52.8 ± 16.8	79.5 ± 19.5	17.0 ± 4.7	-8.5 ± 6.7
Observed mean	0.91 ± 0.15	0.83 ± 0.15	61.6 ± 26.1	71.0 ± 30.8	15.4 ± 6.4	-7.2 ± 9.7
TIE-GCM	0.90	0.78	61.5	61.5	3.8	-7.7

Note. For the crest latitude, negative values mean southward movements. The observed means of $\frac{dN_m F_2}{dF_{10.7}}$ and $\frac{dh_m F_2}{dF_{10.7}}$ are the simple arithmetic averages of the CHAMP, GRACE, and FORMOSAT-3/COSMIC values. The observed mean $\frac{d\theta_m F_2}{dF_{10.7}}$ is the average of the GRACE and FORMOSAT-3/COSMIC values only. The uncertainties of the mean values are the root-mean-squares of the individual ones.

maximum run ($F_{10.7} = 200$ sfu) is also not significant. So the sensitivities derived from the observations and the TIE-GCM benchmark runs can be compared directly.

Ionosonde observations suggest that the solar cycle sensitivity of $N_m F_2$ (hereafter denoted by $\frac{dN_m F_2}{dF_{10.7}}$) at the equator is $\sim 10^{12}$ el $m^{-3}/100F_{10.7}$ (Bum et al., 2011; Liu et al., 2006) and the value of the sensitivity exhibits strong diurnal and seasonal variabilities at higher latitudes (Chen & Liu, 2010; Kalita et al., 2015). We search for the locations of the EIA crests in the annually, zonally averaged satellite RO measurements and find the values of $N_m F_2$. As expected, these $N_m F_2$ values are correlated with the annually averaged $F_{10.7}$. In Figures 5a–5c, the filled circles are for the northern hemispheric EIA crest and the open circles are for the southern hemispheric EIA crest. The solid and dash-dotted lines are the least squares linear regression of the northern and southern hemispheric EIA crests, respectively, giving the estimates of $\frac{dN_m F_2}{dF_{10.7}}$ shown in Table 2. In summary, the satellite observations suggest a mean value of the northern hemispheric $\frac{dN_m F_2}{dF_{10.7}}$ value of 0.91×10^{12} el $m^{-3}/100F_{10.7}$ (a simple arithmetic average of the three measurements) with a 2σ uncertainty 0.15×10^{12} el $m^{-3}/100F_{10.7}$ (obtained by the root mean squares of individual uncertainties). In the southern hemisphere, the value of $\frac{dN_m F_2}{dF_{10.7}}$ is $(0.83 \pm 0.15) \times 10^{12}$ el $m^{-3}/100F_{10.7}$, slightly less than the northern hemispheric value due likely to the transequatorial wind effect described above.

For data-model comparison, we also estimate the values of $\frac{dN_m F_2}{dF_{10.7}}$, based on the two benchmark runs of the TIE-GCM at $F_{10.7} = 70$ sfu and 200 sfu (see Figure 5d). In the solar maximum run, the EIA crest electron densities in the northern and southern hemispheres are 1.49×10^{12} el m^{-3} and 1.33×10^{12} el m^{-3} , respectively. In the solar minimum one, they are 0.32×10^{12} el m^{-3} in both the hemispheres. Thus, the values of $\frac{dN_m F_2}{dF_{10.7}}$ in the TIE-GCM two benchmark runs are 0.90×10^{12} el $m^{-3}/100F_{10.7}$ and 0.78×10^{12} el $m^{-3}/100F_{10.7}$ in the northern and southern hemispheres, respectively, consistent with the observed values. In addition, the interhemispheric asymmetry for the observed $\frac{dN_m F_2}{dF_{10.7}}$ values is also qualitatively reproduced by the TIE-GCM.

The variation of $h_m F_2$ over the solar cycle has been well documented (see the review of, e.g., Hoque & Jakowski, 2012). The increase of $h_m F_2$ during solar maximum is mainly due to the increase in neutral temperature (Garriott & Rishbeth, 1963; Limberger et al., 2015; Qian et al., 2008; Zhang et al., 1999). If the pressure coordinate is used instead of altitude, these peaks would stay close to the pressure level $\sim 5 \times 10^{-8}$ hPa during solar maximum and solar minimum (Rishbeth & Edwards, 1989). Like $N_m F_2$, the solar cycle sensitivity of $h_m F_2$ (hereafter denoted by $\frac{dh_m F_2}{dF_{10.7}}$) varies with local time, seasons, and latitudes. Here we review some of their values derived from ground-based and ionosonde observations. At midlatitudes, Lei et al. (2005) estimated the value of $\frac{dh_m F_2}{dF_{10.7}}$ to be 30–50 km/100 $F_{10.7}$ based on the data over Millstone Hill, USA (43°N). Liu et al. (2006) suggested a value of 35 km/100 $F_{10.7}$ based on the data over Hobart, Australia (43°S) and Kokubunji, Japan (36°N). Similarly, a recent observation over Cyprus (35°N) revealed

an increase of 50 km in $h_m F_2$ at noon time from 2009 to 2013, which gives $\frac{dh_m F_2}{dF_{10.7}}$ of ~ 80 km/100 $F_{10.7}$ (assuming the annual values of $F_{10.7}$ were 70 sfu and 130 sfu in 2009 and 2013, respectively) (Haralambous & Oikonomou, 2015). At subtropical latitudes, observations over New Delhi (28°N) (Sethi et al., 2008) suggested a decrease of 30–40 km in $h_m F_2$ from 2001–2002 to 2004–2005 during the equinox, that is, 40–50 km/100 $F_{10.7}$ (assuming the average values of $F_{10.7}$ were 180 sfu and 100 sfu in 2001 and 2005, respectively). Over Puerto Rico (18°N), the northern EIA region, $\frac{dh_m F_2}{dF_{10.7}}$ lies between 50 and 60 km/100 $F_{10.7}$ (Brum et al., 2011).

Figures 5e–5g shows the values of $h_m F_2$ determined from the GPS RO measurements. The linear regression with $F_{10.7}$ is also shown. The $\frac{dh_m F_2}{dF_{10.7}}$ (km/100 $F_{10.7}$) values obtained are listed in Table 2. Although the associated uncertainty is rather large (the 2σ uncertainty of 50 km/100 $F_{10.7}$ for GRACE), the GPS data consistently suggest that a mean value of $\frac{dh_m F_2}{dF_{10.7}}$ is 60–70 km/100 $F_{10.7}$ in both the hemispheres. The mean of the three measurements is 61.6 ± 26.1 km/100 $F_{10.7}$ at the northern hemispheric EIA crest, which is higher than the value observed over Puerto Rico. The value in the northern hemisphere is slightly lower than that at the southern hemispheric EIA crest (71.0 ± 30.8 km/100 $F_{10.7}$). This upward movement of the EIA crests is reproduced by the TIE-GCM benchmark runs (Figure 5h). In the solar maximum run, the altitudes of the EIA crests in the northern and southern hemispheres are 390 km. In the solar minimum, the corresponding altitudes are 310 km. Thus, these benchmark runs predict $\frac{dh_m F_2}{dF_{10.7}}$ to be 61.5 km/100 $F_{10.7}$ in both the hemispheres, in reasonable agreement with the observed values.

We next quantify the poleward movement of the EIA crests over the solar cycle. The values of $\frac{d\theta_m F_2}{dF_{10.7}}$ (degrees/100 $F_{10.7}$), obtained from the linear regression analysis in Figures 5i–5k, are summarized in Table 2; negative values mean southward movement. Due to poor sampling, CHAMP observations of the EIA movements are subject to large uncertainties and imply no statistically significant movements of the EIA crests. In contrast, the EIA movements in the northern hemisphere derived from GRACE and FORMOSAT-3/COSMIC observations are larger and statistically robust. These two observations suggest a mean movement of the northern hemispheric EIA crest of $15.4^\circ \pm 6.4^\circ/100F_{10.7}$. This value can be compared directly with Kumar et al.'s (2014) observation, in which the movement of the northern hemispheric EIA crest was 4.3° during 2005–2009. Assuming an annual value of $F_{10.7}$ to be 94.5 sfu in 2005 and 70.5 sfu in 2009, the corresponding value of $\frac{d\theta_m F_2}{dF_{10.7}}$ for Kumar et al.'s (2014) observation is $17.9^\circ/100F_{10.7}$, which is about 15% larger than the mean of those from the GRACE and FORMOSAT-3/COSMIC observations. In contrast, the value of $\frac{d\theta_m F_2}{dF_{10.7}}$ reported by Huang and Cheng (1996) is significantly smaller than the value reported here. In the southern hemisphere, only COSMIC/FORMOSAT-3 observed a significant movement of the EIA crest ($-8.5^\circ \pm 6.7^\circ/100F_{10.7}$). GRACE observed a mean movement of $-5.9^\circ/100F_{10.7}$, but the uncertainty is large ($-12.0^\circ/100F_{10.7}$); CHAMP was not able to see measurable movement of the southern EIA crest. Taking the mean of the GRACE and COSMIC/FORMOSAT-3 observation, the observed movement of the southern hemispheric EIA crest over the solar cycle is insignificant ($-7.2^\circ \pm 9.7^\circ/100F_{10.7}$).

TIE-GCM qualitatively reproduces the poleward movement of the northern hemispheric EIA crest (Figure 5l). The latitudes of the EIA crests in the solar maximum run are 16°N and 24°S and those in the solar minimum run are 11°N and 14°S. Thus, the modeled movement of the northern hemispheric EIA crest is $3.8^\circ/100F_{10.7}$, which is much smaller than the observed value. The modeled movement of the southern hemispheric EIA crest is $-7.7^\circ/100F_{10.7}$, which is consistent with the observed mean, even though the observation is not statistically significant.

3.4. Time Evolution Over the 11 Year Solar Cycle

Figure 6a shows the latitudinal evolution of the observed electron density at 305 km. In this figure, the three measurements (CHAMP, GRACE, FORMOSAT-3/COSMIC) have been “merged” into a single data set: on any given day, if more than one instrument provided the measurement of electron density in the regular grids we defined in section 2, then the average of these measurements was taken as the merged value. The averaging was weighted by the number of valid data points provided by the individual instrument on the grids. Note that because of the high sampling rate of FORMOSAT-3/COSMIC, the weighted average is dominated by the FORMOSAT-3/COSMIC measurements in the merged data after 2007. The figure shows that the 11 year

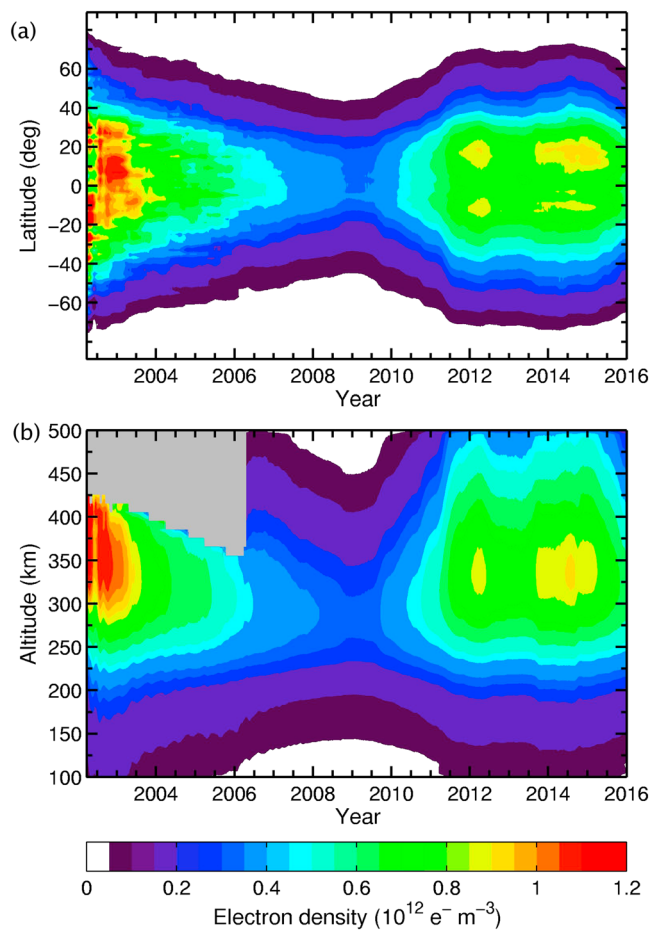


Figure 6. (a) The latitudinal evolution of the ionospheric electron density at 305 km. (b) The vertical evolution of the tropical ionospheric electron density, averaged over 25°S–25°N.

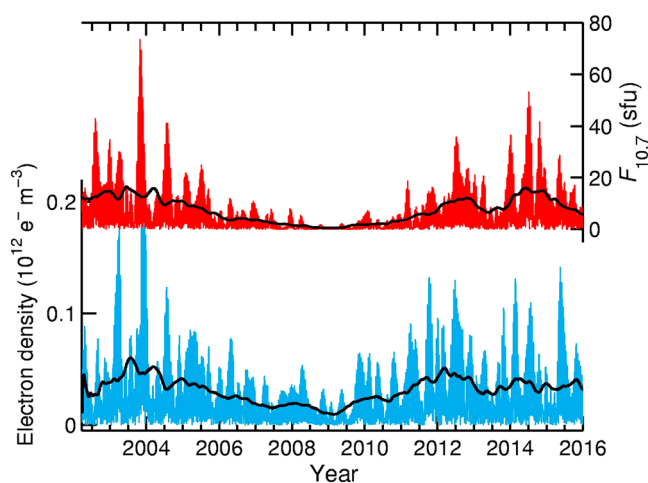


Figure 7. The absolute values of the 27 day FFT-filtered signals (top: $F_{10.7}$; bottom: electron density) at 305 km averaged between 25°S and 25°N. A 1 year running averages are shown by the black solid lines.

solar cycle response in the ionospheric electron density is the most significant at low latitudes 40°S–40°N. The EIA crests at around $\pm 20^\circ$ latitude were clearly observed during the high solar activity period in 2012–2014, whereas the EIA crests were not obvious during the high solar activity period in the early 2002, primarily due to the low sampling rate of CHAMP at that time.

Figure 6b shows the evolution of the vertical profiles of the observed electron density, which is a temporal expansion of Figure 1. The electron density was averaged over 25°S–25°N. The 11 year solar cycle response of the tropical ionospheric electron density is maximized at altitudes between 250 km and 450 km. Consistent with Figure 1, the peak of the tropical electron density is located at 290 km during the low solar activity period in 2009, and the height of the peak is ~ 50 km lower than that during high solar activity periods (2003 and 2014). As discussed in section 3.3, changes in the peak height are primarily due to changes in neutral temperature.

3.5. The 27 Day Solar Cycle Modulation: A Brief Update

Besides the 11 year solar cycle modulation, the decadal observations by CHAMP, GRACE, and FORMOSAT-3/COSMIC also reveal the secondary effect on the 27 day rotational cycle modulation in the ionospheric electron density. The recurrence tendency of EUV and geomagnetic activity by the 27 day period of the solar rotation cause electron density fluctuating at the period as well as the harmonics at lower periods (Lei et al., 2008; Pedatella et al., 2010). Using ionosonde measurements, Ma et al. (2012) showed that the contributions of EUV and geomagnetic activity to the 27 day variations in the peak electron density are comparable in magnitude. The 27 day solar cycle modulation is also apparent in the global electron density (Chen et al., 2015). Liang et al. (2008) established the presence of the solar rotation-induced variability in the first 2 years of FORMOSAT-3/COSMIC data. Here we update Liang et al.'s (2008) results using the merged CHAMP, GRACE, and FORMOSAT-3/COSMIC data set.

The 2-D structure of the 27 day rotational signal in the ionosphere is retrieved using the fast Fourier transform (FFT). A Hanning window with a band-pass domain from 25 to 35 days is applied to retain the 27 day solar signal; periods below 20 days or above 40 days are damped (Kobayashi-Kirschvink et al., 2012). The same FFT filtering window is applied to the $F_{10.7}$ index. We compare the filtered $F_{10.7}$ index with the filtered electron density time series at 305 km averaged between 25°S and 25°N in Figure 7. The absolute values of these FFT-filtered time series are shown. We have chosen to show the absolute values, rather than the original FFT-filtered time series because the amplitude modulation of the 27 day solar response over the 11 year solar cycle can be more clearly shown when a 1 year running average is applied (black solid lines). Both filtered time series show stronger 27 day signals in 2002–2005 and 2012–2014 during high solar activity periods. The 27 day signal in the electron density generally follows that of $F_{10.7}$ in both amplitude and phase, except when the Sun occasionally exhibited strong solar flares, such as those in late 2003 (Tsurutani et al., 2005; Woods et al., 2004).

The latitudinal evolution of the 27 day solar cycle signal is shown in Figure 8a. The pattern is similar to that of the 11 year solar cycle signal in

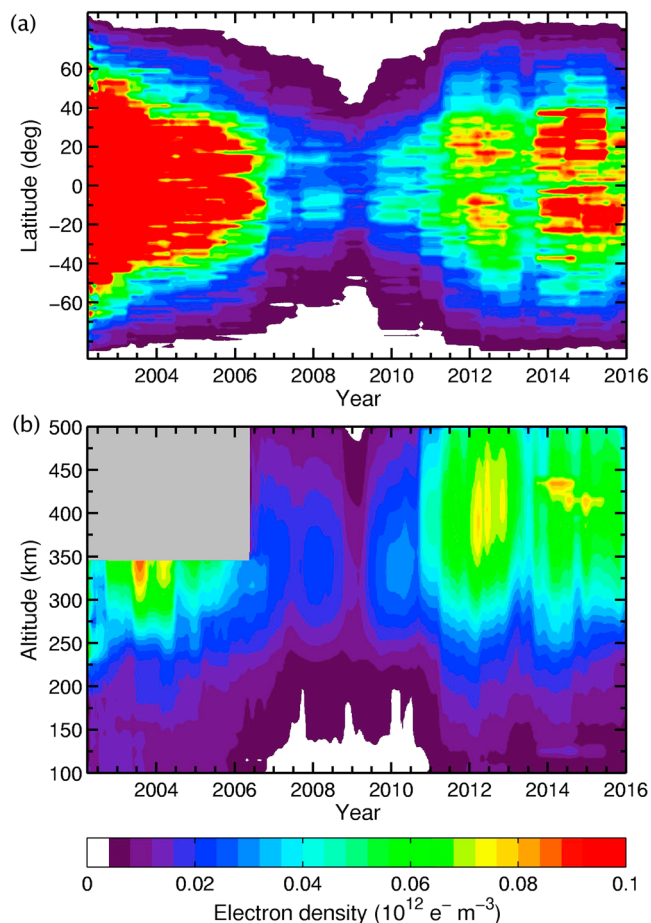


Figure 8. Similar to Figure 6 but for absolute deviation of the 27 day band-pass filtered signal in the ionospheric electron density. A 1 year running average has been applied.

Figure 6a: when the solar cycle is at maximum, the 27 day solar cycle modulation on the ionospheric electron density is also strong because of the inhomogeneous distribution of sunspots on an active Sun's surface that results in a 27 day oscillation in the intensity of the EUV flux. Furthermore, the amplitude of the 27 day response changes with the phase of the 11 year solar cycle.

The vertical evolution of the 27 day solar cycle signal is shown in Figure 8b. Due to missing data, there is no useful signal above 305 km before 2006 (CHAMP period). The pattern is similar to that in Figure 6b except the peak response to the 27 day solar cycle is located at an altitude ~ 50 km higher than that of the 11 year solar cycle. During the high solar activity period (2012–2014), the response to the 27 day solar cycle forcing is most significant between 350 km and 450 km. The limited data obtained by CHAMP between 300 and 350 km during 2002–2006 also supports this finding. To our knowledge, this vertical difference of the 11 year and 27 day solar responses in the ionospheric electron density has not been reported previously. It would be interesting to test whether this vertical difference is related to the different 11 year and 27 day solar responses reported by Chen et al. (2015) in the future.

4. Summary

While most of previous studies focused on local changes observed at ground stations, we have examined the annually and zonally averaged latitudinal-vertical structure of the 11 year solar cycle response in ionospheric electron density using the GPS satellite RO measurements. We have also reexamined the EIA changes associated with the solar cycle that were previously reported from ground observations. Our main findings are summarized below.

1. The zonally averaged tropical electron density near 300 km during high solar activity periods (January–December 2003 and April 2014–March 2015) was 3 times greater than that in 2009 during solar minimum.
2. The EIA in the northern hemisphere during high solar activity periods was more prominent than that in the southern hemisphere. Based on Lin et al.'s (2005) simulation, this interhemispheric asymmetry is due to enhanced neutral equatorial wind during high solar activity periods.
3. The observed climatological values of the sensitivities of the EIA peak density, peak altitude, and peak latitude are $0.9 \pm 0.2 \times 10^{12} \text{ el m}^{-3}/100F_{10.7}$, $61.6 \pm 26.1 \text{ km}/100F_{10.7}$, and $15.4 \pm 6.4^\circ/100F_{10.7}$, respectively, in the northern hemisphere and are $0.8 \pm 0.2 \times 10^{12} \text{ el m}^{-3}/100F_{10.7}$, $71.0 \pm 30.8 \text{ km}/100F_{10.7}$, and $-7.2 \pm 9.7^\circ/100F_{10.7}$ in the southern hemisphere.

In addition, we studied the 27 day solar cycle modulation on the zonally averaged, daily ionospheric electron density profiles. While the amplitude of the 27 day solar variation in the electron density positively correlates with the phase of the 11 year solar cycle, we found that the peak altitude of the 27 day solar cycle response is always located above the electron density peak, regardless of the phase of the solar cycle. During the high solar activity period in 2014, the response of the 27 day signal peaked at ~ 50 km higher in altitude than that of the 11 year solar response.

These observed vertical changes with the solar cycle phase in the ionospheric electron density had not been studied and modeled thoroughly and are potentially valuable for evaluating the performance of current ionosphere models for further elucidating the effects of solar variability on space weather. Extended GPS radio occultation over future solar cycles is critical to resolve the discrepancies between the model predictions and the observations reported and discussed in this work.

Acknowledgments

We thank Irene Chen for reading our manuscript. K. F. L. was supported by the NASA grant NNX14AR40G. L. C. L., X. H. B. and M. C. L. were supported under Ministry of Science and Technology (MOST) grant 105-2111-M-001-006-MY3 to Academia Sinica. We thank TACC/NCAR for providing GPS data. We would like to thank the Editor and two anonymous reviewers for their constructive and insightful comments. $F_{10.7}$ was obtained from ftp://ftp.geolab.nrcan.gc.ca/data/solar_flux/.

References

- Afraimovich, E. L., Astafyeva, E. I., Oinats, A. V., Yasukevich, Y. V., & Zhivetiev, I. V. (2008). Global electron content: A new conception to track solar activity. *Annales de Geophysique*, 26(2), 335–344. <https://doi.org/10.5194/angeo-26-335-2008>
- Alizadeh, M. M., Schuh, H., Todorova, S., & Schmidt, M. (2011). Global ionosphere maps of VTEC from GNSS, satellite altimetry, and Formosat-3/COSMIC data. *Journal of Geodesy*, 85(12), 975–987. <https://doi.org/10.1007/s00190-011-0449-z>
- Anthes, R. A., Ector, D., Hunt, D. C., Kuo, Y.-H., Rocken, C., Schreiner, W. S., ... Yen, N. L. (2008). The COSMIC/FORMOSAT-3 mission: Early results. *Bulletin of the American Meteorological Society*, 89(3), 313–333. <https://doi.org/10.1175/BAMS-89-3-313>
- Appleton, E. V. (1946). Two anomalies in the ionosphere. *Nature*, 157(3995), 691–691. <https://doi.org/10.1038/157691a0>
- Appleton, E. V., & Naismith, R. (1940). Normal and abnormal region-E ionisation. *Proceedings of the Physical Society*, 52(3), 402–415. <https://doi.org/10.1088/0959-5309/52/3/311>
- Araujo-Pradere, E. A., Redmon, R., Fedrizzi, M., Viereck, R., & Fuller-Rowell, T. J. (2011). Some characteristics of the ionospheric behavior during the solar cycle 23–24 minimum. *Solar Physics*, 274(1–2), 439–456. <https://doi.org/10.1007/s11207-011-9728-3>
- Balan, N., Bailey, G. J., & Jayachandran, B. (1993). Ionospheric evidence for a nonlinear relationship between the solar EUV and 10.7 cm fluxes during an intense solar cycle. *Planetary and Space Science*, 41(2), 141–145. [https://doi.org/10.1016/0032-0633\(93\)90043-2](https://doi.org/10.1016/0032-0633(93)90043-2)
- Balan, N., Rajesh, P. K., Sripathi, S., Tulasiram, S., Liu, J. Y., & Bailey, G. J. (2013). Modeling and observations of the north-south ionospheric asymmetry at low latitudes at long deep solar minimum. *Advances in Space Research*, 52(3), 375–382. <https://doi.org/10.1016/j.asr.2013.04.003>
- Baron, M. J., Heinselman, C. J., & Petriceks, J. (1983). Solar cycle and seasonal variations of the ionosphere observed with the Chatanika incoherent scatter radar. *Radio Science*, 18(6), 895–900. <https://doi.org/10.1029/RS018i006p00895>
- Bartels, J. (1950). 27-day variations in F_2 layer critical frequencies at Huancayo. *Journal of Atmospheric and Terrestrial Physics*, 1(1), 2–12. [https://doi.org/10.1016/0021-9169\(50\)90010-9](https://doi.org/10.1016/0021-9169(50)90010-9)
- Bergeot, N., Tsagouri, I., Bruyninx, C., Legrand, J., Chevalier, J. M., Defraigne, P., ... Pottiaux, E. (2013). The influence of space weather on ionospheric total electron content during the 23rd solar cycle. *Journal of Space Weather Space Climate*, 3, A25. <https://doi.org/10.1051/swsc/2013047>
- Bilitza, D., McKinnell, L. A., Reinisch, B., & Fuller-Rowell, T. (2011). The international reference ionosphere today and in the future. *Journal of Geodesy*, 85(12), 909–920. <https://doi.org/10.1007/s00190-010-0427-x>
- Bramley, E. N., & Peart, M. (1965). Diffusion and electromagnetic drift in the equatorial F_2 -region. *Journal of Atmospheric and Terrestrial Physics*, 27(11–12), 1201–1211. [https://doi.org/10.1016/0021-9169\(65\)90081-4](https://doi.org/10.1016/0021-9169(65)90081-4)
- Brum, C. G. M., Rodrigues, F. D., dos Santos, P. T., Matta, A. C., Aponte, N., Gonzalez, S. A., & Robles, E. (2011). A modeling study of f_oF_2 and h_mF_2 parameters measured by the Arecibo incoherent scatter radar and comparison with IRI model predictions for solar cycles 21, 22, and 23. *Journal of Geophysical Research*, 116, A03324. <https://doi.org/10.1029/2010JA015727>
- Chen, Y., & Liu, L. (2010). Further study on the solar activity variation of daytime N_mF_2 . *Journal of Geophysical Research*, 115, A12337. <https://doi.org/10.1029/2010JA015847>
- Chen, Y., Liu, L., Le, H., & Zhang, H. (2015). Discrepant responses of the global electron content to the solar cycle and solar rotation variations of EUV irradiance. *Earth, Planets and Space*, 67(1), 80. <https://doi.org/10.1186/s40623-015-0251-x>
- Dickinson, R. E., Ridley, E. C., & Roble, R. G. (1981). A three-dimensional general circulation model of the thermosphere. *Journal of Geophysical Research*, 86(A3), 1499–1512. <https://doi.org/10.1029/JA086iA03p01499>
- Dickinson, R. E., Ridley, E. C., & Roble, R. G. (1984). Thermospheric general circulation with coupled dynamics and composition. *Journal of the Atmospheric Sciences*, 41(2), 205–219. [https://doi.org/10.1175/1520-0469\(1984\)041%3C0205:TGCWCD%3E2.0.CO;2](https://doi.org/10.1175/1520-0469(1984)041%3C0205:TGCWCD%3E2.0.CO;2)
- Duncan, R. A. (1960). The equatorial F -region of the ionosphere. *Journal of Atmospheric and Terrestrial Physics*, 18(2–3), 89–100. [https://doi.org/10.1016/0021-9169\(60\)90081-7](https://doi.org/10.1016/0021-9169(60)90081-7)
- Fejer, J. A. (1964). Atmospheric tides and associated magnetic effects. *Reviews of Geophysics*, 2(2), 275–309. <https://doi.org/10.1029/RG002i002p00275>
- Forbes, J. M., Palo, S. E., & Zhang, X. (2000). Variability of the ionosphere. *Journal of Atmospheric and Solar-Terrestrial Physics*, 62(8), 685–693. [https://doi.org/10.1016/S1364-6826\(00\)00029-8](https://doi.org/10.1016/S1364-6826(00)00029-8)
- Forbes, J. M., Zhang, X., Palo, S., Russell, J., Mertens, C. J., & Mlynczak, M. (2008). Tidal variability in the ionospheric dynamo region. *Journal of Geophysical Research*, 113, A02310. <https://doi.org/10.1029/2007JA012737>
- Garner, T. W., Gaussiran, T. L., Tolman, B. W., Harris, R. B., Calfas, R. S., & Gallagher, H. (2008). Total electron content measurements in ionospheric physics. *Advances in Space Research*, 42(4), 720–726. <https://doi.org/10.1016/j.asr.2008.02.025>
- Garriott, O. K., & Rishbeth, H. (1963). Effects of temperature changes on the electron density profile in the F_2 -layer. *Planetary and Space Science*, 11(6), 587–590. [https://doi.org/10.1016/0032-0633\(63\)90165-X](https://doi.org/10.1016/0032-0633(63)90165-X)
- Gray, L. J., Beer, J., Geller, M., Haigh, J. D., Lockwood, M., Matthes, K., ... White, W. (2010). Solar influences on climate. *Reviews of Geophysics*, 48(4), RG4001. <https://doi.org/10.1029/2009RG000282>
- Handzo, R., Forbes, J. M., & Reinisch, B. (2014). Ionospheric electron density response to solar flares as viewed by Digisondes. *Space Weather*, 12, 205–216. <https://doi.org/10.1002/2013SW001020>
- Hanson, W. B., & Moffett, R. J. (1966). Ionization transport effects in equatorial F region. *Journal of Geophysical Research*, 71(23), 5559–5572. <https://doi.org/10.1029/JZ071i023p05559>
- Haralambous, H., & Oikonomou, C. (2015). Comparison of peak characteristics of the F_2 ionospheric layer obtained from the Cyprus Digisonde and IRI-2012 model during low and high solar activity period. *Advances in Space Research*, 56(9), 1927–1938. <https://doi.org/10.1016/j.asr.2015.01.036>
- Hochegger, G., Nava, B., Radicella, S., & Leitinger, R. (2000). A family of ionospheric models for different uses. *Physics and Chemistry of the Earth, Part C*, 25(4), 307–310. [https://doi.org/10.1016/S1464-1917\(00\)00022-2](https://doi.org/10.1016/S1464-1917(00)00022-2)
- Hoque, M. M., & Jakowski, N. (2012). A new global model for the ionospheric F_2 peak height for radio wave propagation. *Annales de Geophysique*, 30(5), 797–809. <https://doi.org/10.5194/angeo-30-797-2012>
- Huang, Y.-N., & Cheng, K. (1996). Solar cycle variations of the equatorial ionospheric anomaly in total electron content in the Asian region. *Journal of Geophysical Research*, 101(A11), 24,513–24,520. <https://doi.org/10.1029/96JA01297>
- Huang, H., Chen, Y. D., Liu, L. B., Le, H. J., & Wan, W. X. (2015). An empirical model of the topside plasma density around 600 km based on ROCSAT-1 and Hinotori observations. *Journal of Geophysical Research: Space Physics*, 120, 4052–4063. <https://doi.org/10.1002/2014JA020940>
- Ikubanni, S. O., & Adeniyi, J. O. (2017). Relationship between ionospheric F_2 -layer critical frequency, $F_{10.7}$, and $F_{10.7P}$ around African EIA trough. *Advances in Space Research*, 59(4), 1014–1022. <https://doi.org/10.1016/j.asr.2016.11.013>

- Jakowski, N., Wilken, V., & Mayer, C. (2007). Space weather monitoring by GPS measurements on board CHAMP. *Space Weather*, 5, S08006. <https://doi.org/10.1029/2006SW000271>
- Jakowski, N., Hoque, M. M., & Mayer, C. (2011). A new global TEC model for estimating transionospheric radio wave propagation errors. *Journal of Geodesy*, 85(12), 965–974. <https://doi.org/10.1007/s00190-011-0455-1>
- Jones, M. Jr., Forbes, J. M., Hagan, M. E., & Maute, A. (2013). Non-migrating tides in the ionosphere-thermosphere: In situ versus tropospheric sources. *Journal of Geophysical Research: Space Physics*, 118, 2438–2451. <https://doi.org/10.1002/jgra.50257>
- Jones, M. Jr., Forbes, J. M., & Hagan, M. E. (2016). Solar cycle variability in mean thermospheric composition and temperature induced by atmospheric tides. *Journal of Geophysical Research: Space Physics*, 121, 5837–5855. <https://doi.org/10.1002/2016JA022701>
- Kalita, B. R., Bhuyan, P. K., & Yoshikawa, A. (2015). N_mF_2 and h_mF_2 measurements at 95°E and 127°E around the EIA northern crest during 2010–2014. *Earth, Planets and Space*, 67(1), 186. <https://doi.org/10.1186/S40623-015-0355-3>
- Kendall, P. C. (1962). Geomagnetic control of diffusion in the F_2 region of ionosphere—I. The Form of diffusion operator. *Journal of Atmospheric and Terrestrial Physics*, 24(9), 805–811. [https://doi.org/10.1016/0021-9169\(62\)90201-5](https://doi.org/10.1016/0021-9169(62)90201-5)
- Kobayashi-Kirschvink, K. J., Li, K.-F., Shia, R.-L., & Yung, Y. L. (2012). Fundamental modes of atmospheric CFC-11 from Empirical Mode Decomposition. *Advances in Adaptive Data Analysis*, 04(04), 1250024. <https://doi.org/10.1142/S1793536912500240>
- Kumar, S., Singh, A. K., & Lee, J. (2014). Equatorial Ionospheric Anomaly (EIA) and comparison with IRI model during descending phase of solar activity (2005–2009). *Advances in Space Research*, 53(5), 724–733. <https://doi.org/10.1016/j.asr.2013.12.019>
- Kumar, S., Patel, K., & Singh, A. K. (2016). TEC variation over an equatorial and anomaly crest region in India during 2012 and 2013. *GPS Solutions*, 20(4), 617–626. <https://doi.org/10.1007/s10291-015-0470-4>
- Kutiev, I., Otsuka, Y., Pancheva, D., & Heelis, R. (2012). Response of low-latitude ionosphere to medium-term changes of solar and geomagnetic activity. *Journal of Geophysical Research*, 117, A08330. <https://doi.org/10.1029/2012JA017641>
- Lei, J., Liu, L., Wan, W., & Zhang, S. (2005). Variations of electron density based on long-term incoherent scatter radar and ionosonde measurements over Millstone Hill. *Radio Science*, 40, RS2008. <https://doi.org/10.1029/2004RS003106>
- Lei, J., Thayer, J. P., Forbes, J. M., Wu, Q., She, C., Wan, W., & Wang, W. (2008). Ionosphere response to solar wind high-speed streams. *Geophysical Research Letters*, 35, L19105. <https://doi.org/10.1029/2008GL035208>
- Li, K.-F., Zhang, Q., Tung, K.-K., & Yung, Y. L. (2016). Resolving a long-standing model-observation discrepancy on ozone solar cycle response. *Earth, Space and Science*, 3(10), 431–440. <https://doi.org/10.1002/2016EA000199>
- Liang, M.-C., Li, K.-F., Shia, R.-L., & Yung, Y. L. (2008). Short-period solar cycle signals in the ionosphere observed by FORMOSAT-3/COSMIC. *Geophysical Research Letters*, 35, L15818. <https://doi.org/10.1029/2008GL034433>
- Limberger, M., Hernández-Pajares, M., Aragón-Ángel, A., Altadill, D., & Dettmering, D. (2015). Long-term comparison of the ionospheric F_2 layer electron density peak derived from ionosonde data and Formosat-3/COSMIC occultations. *Journal of Space Weather and Space Climate*, 5, A21. <https://doi.org/10.1051/swsc/2015023>
- Lin, C. H., Richmond, A. D., Heelis, R. A., Bailey, G. J., Lu, G., Liu, J. Y., ... Su, S. Y. (2005). Theoretical study of the low- and midlatitude ionospheric electron density enhancement during the October 2003 superstorm: Relative importance of the neutral wind and the electric field. *Journal of Geophysical Research*, 110, A12312. <https://doi.org/10.1029/2005JA011304>
- Liu, L., Wan, W., Ning, B., Pirog, O. M., & Kurkin, V. I. (2006). Solar activity variations of the ionospheric peak electron density. *Journal of Geophysical Research*, 111, A08304. <https://doi.org/10.1029/2006JA011598>
- Luan, X., Wang, P., Dou, X., & Liu, Y. C.-M. (2015). Interhemispheric asymmetry of the equatorial ionization anomaly in solstices observed by COSMIC during 2007–2012. *Journal of Geophysical Research: Space Physics*, 120, 3059–3073. <https://doi.org/10.1002/2014JA020820>
- Ma, R., Xu, J., Wang, W., & Lei, J. (2012). The effect of ~27 day solar rotation on ionospheric F_2 region peak densities (N_mF_2). *Journal of Geophysical Research*, 117, A03303. <https://doi.org/10.1029/2011JA017190>
- Martyn, D. F. (1955). Theory of height and ionization density changes at the maximum of a Chapman-like region, taking account of ion production, decay, diffusion and total drift. In *Proceedings Cambridge Conference* (pp. 254–259). London, UK: Physical Society.
- Mikhailov, A. V., & Perrone, L. (2015). The annual asymmetry in the F_2 layer during deep solar minimum (2008–2009): December anomaly. *Journal of Geophysical Research: Space Physics*, 120, 1341–1354. <https://doi.org/10.1002/2014JA020929>
- Mitra, S. K. (1946). Geomagnetic control of region F_2 of the ionosphere. *Nature*, 158(4019), 668–669. <https://doi.org/10.1038/158668a0>
- Munro, G. H. (1962). Diurnal variations in the ionosphere deduced from satellite radio signals. *Journal of Geophysical Research*, 67(1), 147–156. <https://doi.org/10.1029/JZ067i001p00147>
- Namba, S., & Maeday, K. I. (1939). *Radio wave propagation* (p. 86). Tokyo: Corona Publishing.
- Nanan, B., Chen, C. Y., Rajesh, P. K., Liu, J. Y., & Bailey, G. J. (2012). Modeling and observations of the low latitude ionosphere-plasmasphere system at long deep solar minimum. *Journal of Geophysical Research*, 117, A08316. <https://doi.org/10.1029/2012JA017846>
- Pedatella, N. M., & Liu, H.-L. (2013). Influence of the El Niño Southern Oscillation on the middle and upper atmosphere. *Journal of Geophysical Research: Space Physics*, 118, 2744–2755. <https://doi.org/10.1002/jgra.50286>
- Pedatella, N. M., Lei, J., Thayer, J. P., & Forbes, J. M. (2010). Ionosphere response to recurrent geomagnetic activity: Local time dependency. *Journal of Geophysical Research*, 115, A02301. <https://doi.org/10.1029/2009JA014712>
- Pedatella, N. M., Yue, X., & Schreiner, W. S. (2015). An improved inversion for FORMOSAT-3/COSMIC ionosphere electron density profiles. *Journal of Geophysical Research: Space Physics*, 120, 8942–8953. <https://doi.org/10.1002/2015JA021704>
- Qian, L., Solomon, S. C., Roble, R. G., & Kane, T. J. (2008). Model simulations of global change in the ionosphere. *Geophysical Research Letters*, 35, L07811. <https://doi.org/10.1029/2007GL033156>
- Rishbeth, H. (1997). The ionospheric E-layer and F-layer dynamos—A tutorial review. *Journal of Atmospheric and Solar-Terrestrial Physics*, 59(15), 1873–1880. [https://doi.org/10.1016/S1364-6826\(97\)00005-9](https://doi.org/10.1016/S1364-6826(97)00005-9)
- Rishbeth, H. (2000). The equatorial F-layer: Progress and puzzles. *Annales de Geophysique*, 18(7), 730–739. <https://doi.org/10.1007/s00585-000-0730-6>
- Rishbeth, H., & Edwards, R. (1989). The isobaric F_2 -layer. *Journal of Atmospheric and Terrestrial Physics*, 51(4), 321–338. [https://doi.org/10.1016/0021-9169\(89\)90083-4](https://doi.org/10.1016/0021-9169(89)90083-4)
- Rishbeth, H., & Mendillo, M. (2001). Patterns of F_2 -layer variability. *Journal of Atmospheric and Solar-Terrestrial Physics*, 63(15), 1661–1680. [https://doi.org/10.1016/S1364-6826\(01\)00036-0](https://doi.org/10.1016/S1364-6826(01)00036-0)
- Roble, R. G., Ridley, E. C., Richmond, A. D., & Dickinson, R. E. (1988). A coupled thermosphere/ionosphere general circulation model. *Geophysical Research Letters*, 15(12), 1325–1328. <https://doi.org/10.1029/GL015i012p01325>
- Scherliess, L., Schunk, R. W., Sojka, J. J., & Thompson, D. C. (2004). Development of a physics-based reduced state Kalman filter for the ionosphere. *Radio Science*, 39, RS1504. <https://doi.org/10.1029/2002RS002797>
- Schreiner, W., Rocken, C., Sokolovskiy, S., Syndergaard, S., & Hunt, D. (2007). Estimates of the precision of GPS radio occultations from the COSMIC/FORMOSAT-3 mission. *Geophysical Research Letters*, 34, L04808. <https://doi.org/10.1029/2006GL027557>

- Sethi, N. K., Dabas, R. S., & Sharma, K. (2008). Comparison between IRI predictions and digital ionosonde measurements of $h_m F_2$ at New Delhi during low and moderate solar activity. *Journal of Atmospheric and Solar-Terrestrial Physics*, 70(5), 756–763. <https://doi.org/10.1016/j.jastp.2007.10.009>
- Shaikh, M. M., Notarpietro, R., & Nava, B. (2014). The impact of spherical symmetry assumption on radio occultation data inversion in the ionosphere: An assessment study. *Advances in Space Research*, 53(4), 599–608. <https://doi.org/10.1016/j.asr.2013.10.025>
- Solomon, S. C., & Qian, L. (2005). Solar extreme-ultraviolet irradiance for general circulation models. *Journal of Geophysical Research*, 110, A10306. <https://doi.org/10.1029/2005JA011160>
- Solomon, S. C., Qian, L., & Burns, A. G. (2013). The anomalous ionosphere between solar cycles 23 and 24. *Journal of Geophysical Research*, 118(10), 6524–6535. <https://doi.org/10.1002/jgra.50561>
- Syndergaard, S., Schreiner, W. S., Rocken, C., Hunt, D. C., & Dymond, K. F. (2006). Preparing for COSMIC: Inversion and analysis of ionospheric data products. In U. Foelsche, G. Kirchengast, & A. Steiner (Eds.), *Atmosphere and climate: Studies by occultation methods* (pp. 137–146). Berlin: Springer. https://doi.org/10.1007/3-540-34121-8_12
- Tapley, B. D., Bettadpur, S., Watkins, M., & Reigber, C. (2004). The gravity recovery and climate experiment: Mission overview and early results. *Geophysical Research Letters*, 31, L09607. <https://doi.org/10.1029/2004GL019920>
- Tsurutani, B. T., Judge, D. L., Guarnieri, F. L., Gangopadhyay, P., Jones, A. R., Nuttall, J., ... Viereck, R. (2005). The October 28, 2003 extreme EUV solar flare and resultant extreme ionospheric effects: Comparison to other Halloween events and the Bastille Day event. *Geophysical Research Letters*, 32, L03509. <https://doi.org/10.1029/2004GL021475>
- Vila, P. (1971). Intertropical F_2 ionization during June and July 1966. *Radio Science*, 6(7), 689–697. <https://doi.org/10.1029/RS006i007p00689>
- Walterscheid, R. L. (1989). Solar cycle effects on the upper atmosphere: Implications for satellite drag. *Journal of Spacecraft and Rockets*, 26(6), 439–444. <https://doi.org/10.2514/3.26089>
- Wang, S., Huang, S., Fang, H., & Wang, Y. (2016). Evaluation and correction of the IRI2016 topside ionospheric electron density model. *Advances in Space Research*, 58(7), 1229–1241. <https://doi.org/10.1016/j.asr.2016.06.020>
- Wells, H. W. (1943). Effects of solar activity on the ionosphere and radio communications. *Proceedings of the IRE*, 31(4), 147–157. <https://doi.org/10.1109/JRPROC.1943.229732>
- Woods, T. N., Eparvier, F. G., Fontenla, J., Harder, J., Kopp, G., McClintock, W. E., ... Snow, M. (2004). Solar irradiance variability during the October 2003 solar storm period. *Geophysical Research Letters*, 31, L10802. <https://doi.org/10.1029/2004GL019571>
- Xiong, C., Park, J., Luhr, H., Stolle, C., & Ma, S. Y. (2010). Comparing plasma bubble occurrence rates at CHAMP and GRACE altitudes during high and low solar activity. *Annales Geophysicae*, 28(9), 1647–1658. <https://doi.org/10.5194/angeo-28-1647-2010>
- Yue, X., Schreiner, W. S., Rocken, C., & Kuo, Y.-H. (2011). Evaluation of the orbit altitude electron density estimation and its effect on the Abel inversion from radio occultation measurements. *Radio Science*, 46, RS1013. <https://doi.org/10.1029/2010RS004514>
- Yue, X., Schreiner, W. S., Kuo, Y.-H., Hunt, D. C., Wang, W., Solomon, S. C., ... Wickert, J. (2012). Global 3-D ionospheric electron density reanalysis based on multisource data assimilation. *Journal of Geophysical Research*, 117, A09325. <https://doi.org/10.1029/2012JA017968>
- Yue, X., Schreiner, W. S., Pedatella, N. M., Anthes, R. A., Mannucci, A. J., Straus, P. R., & Liu, J. (2014). Space weather observations by GNSS radio occultation: From FORMOSAT-3/COSMIC to FORMOSAT-7/COSMIC-2. *Space Weather*, 12, 616–621. <https://doi.org/10.1002/2014SW001133>
- Zhang, S., Fukao, S., Oliver, W. L., & Otsuka, Y. (1999). The height of the maximum ionospheric electron density over the MU radar. *Journal of Atmospheric and Solar-Terrestrial Physics*, 61(18), 1367–1383. [https://doi.org/10.1016/S1364-6826\(99\)00088-7](https://doi.org/10.1016/S1364-6826(99)00088-7)
- Zhou, Y.-L., Wang, L., Xiong, C., Luhr, H., & Ma, S.-Y. (2016). The solar activity dependence of nonmigrating tides in electron density at low and middle latitudes observed by CHAMP and GRACE. *Annales Geophysicae*, 34(4), 463–472. <https://doi.org/10.5194/angeo-34-463-2016>